

Accepted Article Preview: Published ahead of advance online publication



Refractive Index and Thickness Measurements with Ultrahigh Sensitivity via Versatile Surface Plasmon Resonance Holographic Microscope

Lingke Wang, Jingyu Mi, Jiahao Li, Wenrui Li, Siqing Dai, Jiwei Zhang, and Jianlin Zhao

Cite this article as: Lingke Wang, Jingyu Mi, Jiahao Li, Wenrui Li, Siqing Dai, Jiwei Zhang, Jianlin Zhao. Refractive Index and Thickness Measurements with Ultrahigh Sensitivity via Versatile Surface Plasmon Resonance Holographic Microscope. *Light: Advanced Manufacturing* accepted article preview 3 April, 2026; doi: 10.37188/lam.2026.056

This is a PDF file of an unedited peer-reviewed manuscript that has been accepted for publication. LAM are providing this early version of the manuscript as a service to our customers. The manuscript will undergo copyediting, typesetting and a proof review before it is published in its final form. Please note that during the production process errors may be discovered which could affect the content, and all legal disclaimers apply.

Received 6 February 2026; revised 2 April 2026; accepted 3 April 2026;
Accepted article preview online 3 April 2026

Refractive Index and Thickness Measurements with Ultrahigh Sensitivity via Versatile Surface Plasmon Resonance Holographic Microscope

Lingke Wang^{1,2}, Jingyu Mi^{1,2}, Jiahao Li^{1,2}, Wenrui Li^{1,2}, Siqing Dai^{1,2}, Jiwei Zhang^{1,2*}, and Jianlin Zhao^{1,2*}

¹ Key Laboratory of Light Field Manipulation and Information Acquisition, Ministry of Industry and Information Technology, and Shaanxi Key Laboratory of Optical Information Technology, Xi'an, 710129, China

² School of Physical Science and Technology, Northwestern Polytechnical University, Xi'an, 710129, China

* E-mail: jwzhang@nwpu.edu.cn; jlzhao@nwpu.edu.cn

Abstract

Employing optical microscopy for visualisation and quantification of dielectric analytes in the near-field area has been a persistent objective, connecting nanoscale dynamics with macroscopic phenomena. Surface plasmon resonance holographic microscopy (SPRHM) leverages evanescent-field interactions and digital holography to enable label-free wide-field quantitative intensity and phase imaging of the near-field area. With an exceptional sensitivity to changes in refractive index (RI), SPRHM evolved as a flexible tool for high-throughput visualisation and detection of interface reactions, which are always accompanied by variations in RI or thickness of samples. Currently, SPRHM is evolving towards application-oriented deployments across interdisciplinary fields. However, current SPRHM demodulation methods remain insufficient to meet the growing demand for a higher measurement sensitivity. Here, we introduce an optimised Ag–Au bilayer SPR excitation configuration and angle-scanning thickness demodulation workflow, designed to achieve ultrahigh-sensitivity RI and thickness measurements, respectively. Experiment results demonstrate the superior performance of the proposed methods: monitoring of RI variations of ethanol–water evaporation dynamics with a

RI measurement resolution of 2.58×10^{-7} RIU and thickness profiling of a graphene terrace specimen with a step-height accuracy of 0.56 nm. Integrated with these advanced methods, we present a versatile surface plasmon resonance holographic microscope prototype that features minimal opto-mechanical complexity, operational simplicity, and exceptional stability. We believe that this microscope, offering an ultrahigh sensitivity in both RI and thickness measurements, will enable unprecedented observations of biomolecular interactions, nanomaterial optics, electrochemical dynamic processes, etc.

Introduction

Precise visualisation and quantification of the intrinsic physical features of diverse analytes with a high sensitivity are crucial in chemistry, life sciences, and physics to elucidate the underlying mechanisms, as well as in advanced manufacturing technologies to monitor and enhance the production quality. Over the past decades, surface plasmon resonance microscopy (SPRM) has emerged as a powerful imaging platform for analyte detection and label-free characterisation¹. SPRM serves as a spatially resolved evanescent sensing technique based on surface plasmon resonance (SPR), which refers to the collective oscillations of free electrons at a metal–dielectric interface induced by electromagnetic wave coupling². SPR excitation converts incident photons into the generated propagating surface plasmon polariton (SPP)³, causing large complex reflectance changes. The signal shift is very sensitive to changes in refractive index (RI) or thickness near the metal/dielectric interface (the detailed mathematical derivation of the SPR sensing principle is provided in Supplementary Information 1). This enables SPRM with an excellent capability for label-free and high-sensitivity detection of chemical and biological reactions at the surface, which are always accompanied by variations in RI or thickness. Since the introduction of SPRM in 1987⁴, this type of evanescent sensing and imaging platform has been extensively applied in single-molecular⁵/single-cell analysis⁶, biological sensing^{7,8}, dynamic electrochemical reaction detection⁹, and photocatalytic activity monitoring¹⁰. SPRM can be constructed with either a prism coupler¹¹ or an objective with a high numerical aperture¹². Objective-coupled SPRM achieves a superior lateral resolution and aberration-free imaging, outperforming prism-coupled configurations for nanoscale target characterisation. There have been numerous reports on four SPRM schemes involving the

measurement of intensity¹³ or phase¹⁴ variations and resonance shifts in angle¹⁵ or wavelength¹⁶. The intensity detection approach is less sensitive, whereas the angle and wavelength interrogation methods are typically costly and necessitate complex data processing. Phase detection methods deliver a superior sensitivity with respect to the other three methods due to drastic phase responses under SPR¹⁷. SPR phase interrogation theoretically enables RI measurement with an ultrahigh sensitivity of approximately 10^{-8} RIU. However, such values were predicted based on fundamental phase measurement limits and have not been experimentally realised¹⁸⁻²⁰.

In order to exploit the complementary nature of intensity and phase detection mechanisms, surface plasmon resonance holographic microscopy (SPRHM) was developed to acquire intensity and phase images simultaneously by measuring the complex amplitude of reflected light using digital holographic microscopy (DHM)²¹. Compared with intensity-only SPRM, SPRHM offers a better throughput capacity by providing a quantitative access to both phase and intensity²². This enables SPRHM to extract quantitative properties of analytes with higher measurement sensitivity and accuracy and even demodulate two or more physical characteristics simultaneously^{23,24}. Additionally, the numerical refocusing capability of DHM allows SPRHM to increase the data utility significantly and even enable volumetric reconstruction²⁵.

Early SPRHM setups employed two-arm interferometers^{14,26}, suffering from measurement instability from thermal/mechanical drift in the separated object and reference arms. Zhang *et al.* subsequently discussed the common-path off-axis DHM configuration that intrinsically compensates environmental disturbances with an enhanced stability²⁷. Based on this methodology, a compact SPRHM with a common-path interference configuration was proposed by merely incorporating a Wollaston prism into the fundamental SPRM structure²⁸. Benefiting from the noninvasiveness, label-free process, wide field, high throughput, and high sensitivity, common-path objective-coupled SPRHM has been employed to characterise the thickness of two-dimensional (2D) materials²⁸, measure the cell–substrate adhesion gap²⁹, investigate the response of biological specimens to optical force stimuli³⁰, demodulate the cytoplasm RI and cell-substrate distance simultaneously²³, and dynamically monitor the evolution of cellular states under different external stimulations³¹. Nevertheless, existing SPRHM techniques are

still limited in addressing the growing need for a higher measurement sensitivity.

In this study, we propose a Ag–Au bilayer SPR excitation configuration with an optimised layer thicknesses to achieve dynamic RI monitoring with a measurement resolution of 2.58×10^{-7} RIU during ethanol–water mixture evaporation, significantly surpassing the experimental sensitivity (10^{-4} RIU²⁰) of conventional SPR sensing techniques. Furthermore, we introduce an angle-scanning thickness demodulation workflow, enabling an atomic-scale thickness profiling with a resolution of 0.56 nm on a graphene terrace specimen, achieving an accuracy comparable to that of atomic force microscopy (AFM). Moreover, current SPRHM implementations suffer from the following limitations. (1) The use of independent mounts for each optical element makes the setup susceptible to element-specific drift and vibration, which inherently compromises the measurement accuracy and critically limits the performance in ultrasensitive applications. (2) High cleanliness and vibration isolation are demanded, which are rarely achievable outside specialised laboratories. To further improve the measurement stability and system simplicity, we developed a SPR holographic microscope to offer an easy-to-implement and cost-effective solution that significantly enhances the adaptability of SPRHM. As the first product-ready SPR holographic microscope bridging laboratory innovation and industrial applications, the prototype is expected to have a key role in biological research, nanomaterial inspection, and electrochemical studies.

Results

RI measurement with an ultrahigh resolution of 10^{-7} RIU

To further advance the RI measurement sensitivity, we implemented an optimised Ag–Au bilayer SPR excitation configuration in our microscope platform. The thicknesses of the Ag and Au layers were computationally optimised with the custom algorithm. The optimised Ag–Au bilayer SPR excitation configuration could simultaneously achieve a high measurement sensitivity and long-term deployment stability, which neither the Ag nor the Au monolayer can provide alone. This strategy leads to an ultrahigh RI measurement resolution of 10^{-7} RIU. To the best of our knowledge, this is the first demonstration of the theoretical limit in a practical SPR sensor. Furthermore, the flat bilayer configuration eliminates nanofabrication barriers without compromising the performance.

We construct a four-layer SPR excitation configuration consisting of coverslip–Ag-layer–Au-layer–dielectric sample, as shown in Fig. 1a. The Ag layer induces an enhanced RI measurement sensitivity due to the superior SPR excitation efficiency, while the overlying Au layer prevents Ag film oxidation and ensures chemical stability and biocompatibility. With known dielectric constants ε_p , ε_{Ag} , and ε_{Au} (denotes the dielectric constant of the coverslip, Ag-layer, and Au-layer, respectively) and the initial sample RI n_s as the baseline for calculation, we optimise the layer thicknesses of Ag and Au, d_{Ag} and d_{Au} , to provide an ultrahigh RI measurement sensitivity. The layer thickness optimisation algorithm proceeds as follows.

Step 1: The curve of reflection phase shift ϕ versus sample RI n_s under SPR conditions is calculated using the Fresnel formula. The RI measurement sensitivity S is defined as the maximum value of $|\partial\phi/\partial n_s|$, derived from the first derivative of this curve (Fig. 1b).

Step 2: The thicknesses of Ag and Au layers are scanned from 1 to 50 nm with increments of 1 nm, and the angular-dependent reflectance spectra are calculated using the Fresnel formula. The resonance angle θ_R at minimum reflectance for each thickness combination is then extracted (Fig. 1d).

Step 3: S is calculated for each thickness combination while the corresponding θ_R is set as the incidence angle. The optimal layer thicknesses d_{Ag}^* and d_{Au}^* corresponding to maximum S are determined from the sensitivity map (Fig. 1e). θ_R for this optimal bilayer is denoted as θ_R^* .

Step 4: With optimised parameters d_{Ag}^* , d_{Au}^* , and θ_R^* , ϕ versus n_s is calculated using the Fresnel formula for two cases, where the dielectric sample to be measured and air are treated as the fourth layer of the SPR excitation configuration. The RI demodulation curve is then defined as the reflection phase shift difference φ ($\phi_{\text{sample}} - \phi_{\text{air}}$) versus n_s (Fig. 1c).

The above optimisation procedure is conducted through numerical simulations. After identification of the optimal layer thicknesses, the corresponding Ag–Au bilayer SPR excitation configuration is subsequently fabricated.

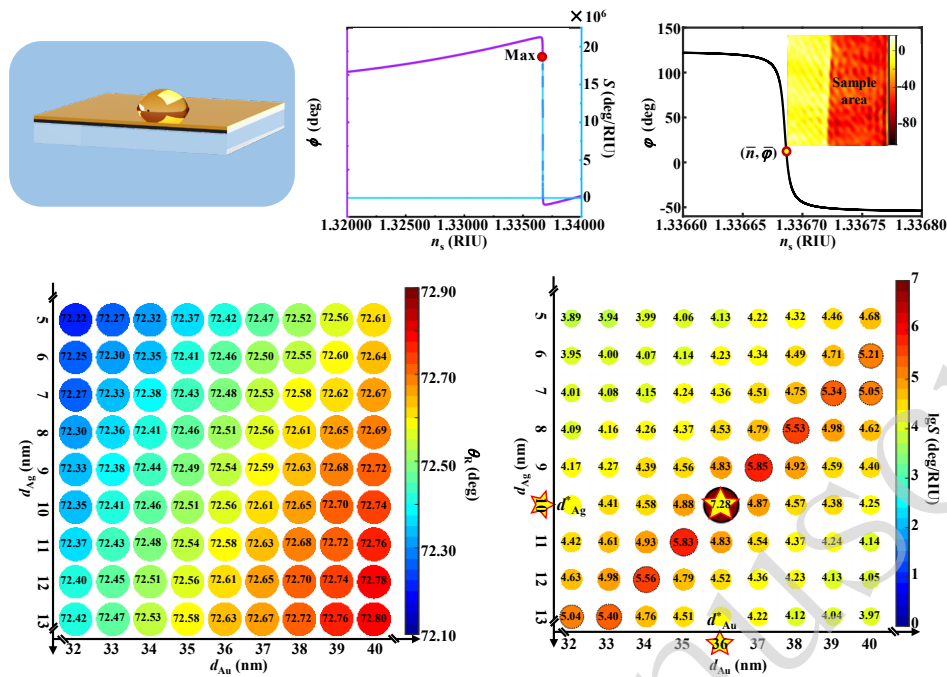


Fig. 1 Ag–Au bilayer SPR excitation configuration and layer thickness optimisation algorithm. **a** Schematic of the four-layer SPR excitation configuration. **b** Definition of RI measurement sensitivity $S: \text{Max}|\partial\phi/\partial n_s|$. The purple line shows the reflection phase shift (ϕ) vs. sample RI (n_s), while the blue indicates the first-order derivative $|\partial\phi/\partial n_s|$. **c** RI demodulation curve of reflection phase shift difference ϕ vs n_s . The inset shows a representative reconstructed phase image. **d,e** SPR resonance angles and S (logarithmic scale) for different Ag–Au layer thicknesses. The optimal layer thicknesses of Ag and Au correspond to the maximum S .

We validated the performance of the designed SPR excitation configuration by monitoring micro-RI changes when evaporating ethanol–water mixtures with various mass concentrations. For the 8.0 wt% mixture (initial RI = 1.3367 at 632.8 nm, interpolated from RI data for aqueous solutions in a chemical handbook³²), the thickness optimisation algorithm yielded a Ag–Au bilayer with thicknesses of 10 and 36 nm, respectively. The optimised metal bilayer was deposited on top of a cleaned coverslip via electron-beam evaporation and integrated into the SPR holographic microscope. This optimised Ag–Au bilayer SPR excitation configuration remains effective for dielectric media with comparable RIs, e.g. mixtures with similar mass concentrations. To validate this robustness, we selected two analogous ethanol–water mixtures with similar mass concentrations (7.5 and 8.4 wt%) for a comparative verification. Using the

double-exposure method, we measured time-varying φ during the volatilisation of mixtures. The φ data underwent an additional correction operation (Supplementary Information 2) and were converted to RI values (at 632.8 nm) using a demodulation curve, as shown in Fig. 2.

As shown in Fig. 2a, φ exhibited a significant monotonic increase over time, contrasting with the pure water's stable fluctuations around a baseline value. This divergence stemmed from the ethanol volatilisation-driven RI reduction, which induced the increase in φ . Conversely, the pure water maintained a constant RI, resulting in φ stability. To demonstrate the ultrahigh sensitivity of our Ag–Au bilayer SPR excitation configuration, we compared its φ dynamics during the 8.0 wt% mixture volatilisation against that obtained by using a standard single Au layer SPR excitation configuration (Fig. 2b). The optimised metal bilayer exhibited $\Delta\varphi = 6.96^\circ$ versus 0.77° for the single Au layer, achieving a nine-fold enhancement. Figure 2c quantifies the time-resolved RI reduction in ethanol–water mixtures with varying mass concentrations. All concentrations exhibited a monotonic RI decrease due to the ethanol volatilisation. For validation, a secondary concentration series (3.5, 4.0, 4.6 wt%) was measured with 4.0 wt% as the baseline (Supplementary Information 3); the results revealed a similar trend. Notably, sporadic RI increases (7.7% of data points) correlated with phase measurement fluctuations ($\sigma = 0.59^\circ$, Supplementary Information 4), likely induced by camera readout perturbations.

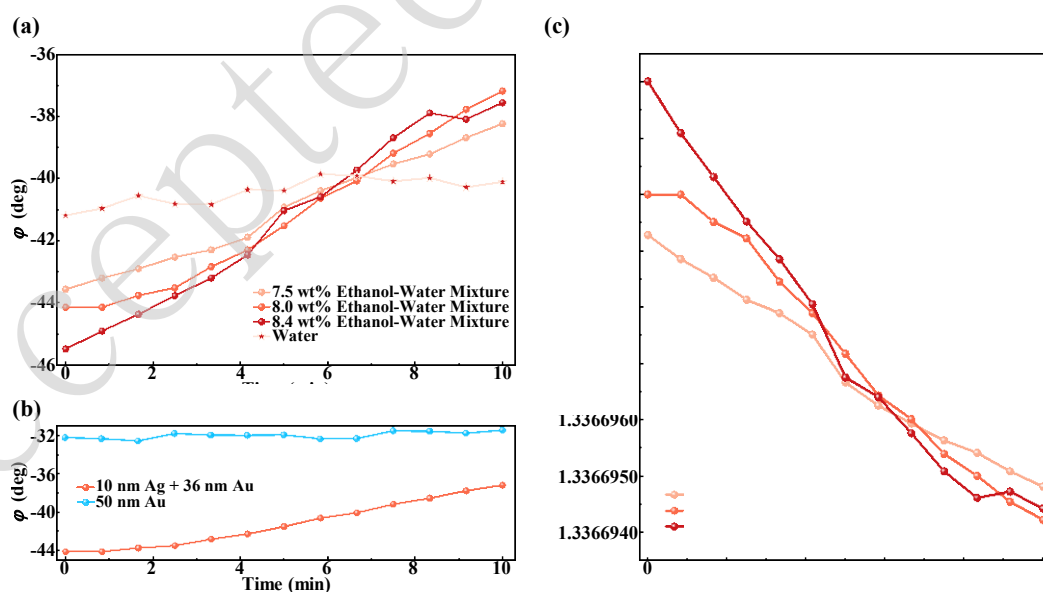


Fig. 2 Measurement results of ethanol–water mixtures obtained using the microscope. **a** Reflection phase shift difference φ variation with time for ethanol–water mixtures with mass concentrations of

7.5, 8.0, and 8.4 wt%, and pure water. **b** Comparison of ϕ variations during the volatilisation of the 8.0 wt% mixture between the standard 50 nm Au and optimised Ag (10 nm)–Au (36 nm) bilayer SPR excitation configuration. The optimised Ag–Au bilayer exhibits a nine-fold enhancement in the variation in ϕ compared to that obtained by using the standard Au layer. **c** Demodulated small RI (at 632.8 nm) changes over time for ethanol–water mixtures with mass concentrations of 7.5, 8.0, and 8.4 wt%.

Table 1 summarises key measurement metrics derived from our experiments. The results indicate that higher mass concentrations of the ethanol–water mixtures lead to larger reflection phase shift difference changes $\Delta\phi$ and larger net RI changes Δn_s over identical durations, correlating with accelerated RI reduction rates. By computing the differential RI between adjacent timepoints and averaging across all measurements, we achieve a consistent RI measurement resolution of 10^{-7} RIU across all six trials. The optimal resolution reaches 2.58×10^{-7} RIU. The RI measurement sensitivity $S = \Delta\phi/\Delta n_s$ was calculated by the measured $\Delta\phi$ – Δn_s pairs. For the 8.0 wt% mixture, the theoretical and experimental S values were 1.90×10^7 deg/RIU and 1.24×10^6 deg/RIU, respectively. This discrepancy stems from the limited dynamic range (8 bit) of the charge-coupled device (CCD), constraining the phase measurements and capping S of the current platform at $\sim 10^6$ deg/RIU. For the 4.0 wt% mixture, the theoretical S was 2.32×10^6 deg/RIU, which was within the platform limits and consistent with the experimental value of 1.71×10^6 deg/RIU. The conventional 50 nm Au layer achieved S of only $\sim 10^4$ deg/RIU. The determination of the optimal thicknesses of the Ag–Au bilayer via our computational optimisation algorithm requires a priori knowledge of the dielectric medium's initial RI (or its approximate range). This constraint establishes our method to be ideal for ultrahigh-sensitivity RI monitoring in dynamic processes, particularly those involving continuous concentration changes. Nevertheless, a fundamental limitation arises if the RI change exceeds the inherently constrained dynamic range of the proposed SPR excitation configuration, beyond which the accurate RI retrieval fails. Notably, the RI dynamic range of the proposed SPR excitation configuration is limited to approximately 10^{-6} RIU, as indicated by Δn_s , which is significantly narrower than that achievable with conventional angular or wavelength interrogation schemes (>0.1 RIU)¹⁷. This restriction originates from the

fundamental trade-off between the realisation of an ultrahigh sensitivity and maintenance of a wide dynamic range in RI sensing systems.

Table 1 Quantitative comparison of measurement metrics for ethanol–water mixtures with different mass concentrations.

SPR excitation configuration	Mass concentrations (wt%)	$\Delta\phi$ (deg)	Ratio of $\Delta\phi$	Δn_s (RIU)	Resolution (RIU)	S (deg/RIU)
10 nm Ag + 36 nm Au	7.5	5.33	\	4.47×10^{-6}	3.73×10^{-7}	1.22×10^6
	8.0	6.96	9.0	5.78×10^{-6}	4.82×10^{-7}	Theory 1.90×10^7
	8.4	7.93	\	7.59×10^{-6}	6.33×10^{-7}	Experiment 1.24×10^6
	8.4	7.93	\	7.59×10^{-6}	6.33×10^{-7}	1.20×10^6
48 nm Ag + 3 nm Au	0.0 (Water)	1.08	\	\	\	\
	3.5	5.52	\	3.25×10^{-6}	2.58×10^{-7}	1.71×10^6
	4.0	6.89	2.6	4.04×10^{-6}	3.37×10^{-7}	Theory 2.32×10^6
	4.6	9.90	\	5.81×10^{-6}	4.84×10^{-7}	Experiment 1.71×10^6
50 nm Au	0.0 (Water)	0.50	\	\	\	\
	4.0	2.61	\	\	\	2.23×10^4
	8.0	0.77	\	\	\	2.15×10^4

Figure 3 quantifies the evaporation kinetics of the ethanol–water mixtures. We establish a linear relationship between the RI reduction rate dn_s/dt (RIU/min) and ethanol mass concentration M (wt%): $dn_s/dt = aM + b$. The linear regression yields coefficients $a' = 3.43 \times 10^{-7}$ and $a'' = 2.35 \times 10^{-7}$ for the two groups of mixtures, showing no significant difference. This consistency arises because both groups share identical solute–solvent interactions (ethanol–water), exhibiting equivalent evaporation kinetics under the same experimental conditions.

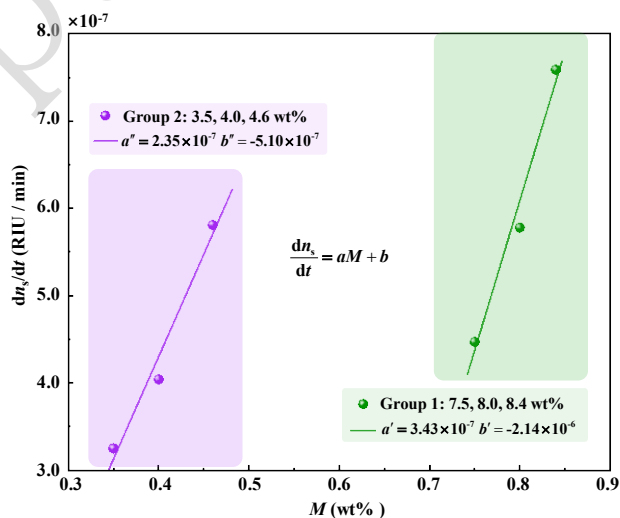


Fig. 3 Evaporation kinetics modelling of ethanol–water mixtures.

Thickness profiling of a 2D material with a subnanometre resolution

To circumvent the technical challenge of a low measurement throughput and establish a novel paradigm for 2D material metrology, we deploy an angle-scanning thickness demodulation workflow on our SPR holographic microscope. The approach enables a rapid, wide-field, and contact-free thickness profiling of 2D materials with a high sensitivity and subnanometre accuracy of 0.56 nm, demonstrated on a graphene terrace and cross-validated with AFM. In addition, it offers an improved measurement throughput without the need for prior empirical calibration.

First, we model a five-layer SPR excitation configuration of glass–Cr-film–Au-layer–2D-material–dielectric (Fig. 4a). According to the Fresnel formula, the reflection phase shift ϕ becomes exclusively dependent on the 2D material thickness d_4 when the wavelength and incidence angle of the illumination light beam, dielectric constants, and thicknesses of the layers in the SPR excitation configuration are fixed. As SPR generates an extreme phase sensitivity to small variations in the specimen's physical parameters, incidence angle scanning is necessary to identify the resonance angle θ_{SPR} for different areas of the inhomogeneous specimen. The angular interrogation is accomplished by adjusting the lateral displacement of the motorised vertical translation stage of the microscope, and a θ -dependent hologram sequence is recorded simultaneously. By extracting the intensity variation of a fixed pixel across the image sequence, the reflectivity is obtained, and θ_{SPR} is identified at minimum reflectivity (Fig. 4b). Once θ_{SPR} is determined, it is set as an incidence angle. The Fresnel formula is employed to calculate ϕ_{air} and ϕ_{water} versus d_4 for air and water as the fifth dielectric layer, respectively. The thickness demodulation curve is then defined as the reflection phase shift difference ϕ ($\phi_{\text{air}} - \phi_{\text{water}}$) against d_4 , as shown in Fig. 4c. Furthermore, pixelwise thickness demodulation is performed on the reconstructed phase distribution derived from the hologram recorded precisely at θ_{SPR} . A statistical analysis of the thickness map yields a histogram that undergoes Gaussian fitting, thus enabling precise determination of the geometric thickness of 2D materials with nanoscale accuracy.

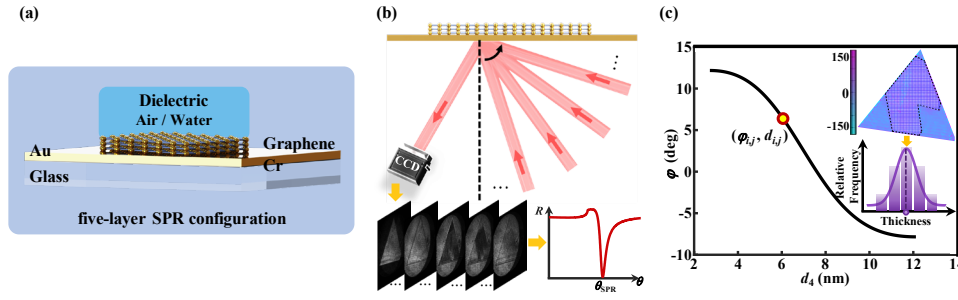


Fig. 4 Angle-scanning thickness demodulation workflow. **a** Construction of a five-layer SPR excitation configuration: glass–Cr–Au–graphene–dielectric (air or water). **b** Recording of hologram sequences followed by angular interrogation and identification of the resonance angle at the minimum reflectivity. **c** Calculation of the thickness demodulation curve (reflection phase shift difference ϕ vs 2D material thickness d_4). The inset shows a reconstructed SPR phase image of graphene. The thickness is determined via pixelwise demodulation and Gaussian fitting.

To evaluate the accuracy of the proposed workflow for thickness profiling of 2D materials, we performed tests on a graphene terrace specimen fabricated via mechanical exfoliation. Prior to the transfer, a 1 nm chromium adhesion layer and 50 nm gold film were deposited onto a cleaned glass coverslip by electron-beam evaporation. The bright-field microscope image in Fig. 5a shows the graphene specimen comprising three distinct step areas of varying thickness. Cross validation was first conducted using a commercial AFM, which characterised the same areas and established reference thicknesses of 5.70, 6.28, and 7.92 nm (Fig. 5b). In the SPR excitation configuration, the model parameters were set as $\epsilon_{\text{glass}} = 2.2955$, $\epsilon_{\text{Cr}} = -1.1305 + 20.818i$, $\epsilon_{\text{Au}} = -11.740 + 1.2611i$, and $\epsilon_{\text{dielectric}} = 1.0/1.7734$ (air or water), based on the values reported by Polyanskiy³³. The dielectric constant of graphene was set to $\epsilon_{\text{graphene}} = 7.6805 + 6.8922i$, according to Bruna and Borini³⁴. The illumination wavelength was fixed at 632.8 nm. The microscope's motorised incidence angle scanning mode was employed to determine θ_{SPR} for the three step areas. The measurement results were 45.45°, 45.73°, and 46.58° for the areas of 5.70, 6.28, and 7.92 nm, respectively. Subsequent calculations of the thickness demodulation curves based on these values, combined with pixelwise demodulation and Gaussian fitting of the measured phase distributions, yielded thickness measurement values of 5.44, 6.00, and 7.62 nm (Fig. 5c). These results show an excellent agreement with the AFM results, with absolute errors below 0.30 nm. This difference could be attributed to the fabrication quality of the

metallic layers and roughness of the substrate. To further evaluate the thickness profiling resolution, step-height differences between adjacent areas were compared. AFM measurement results indicated differences of 0.58 nm (between areas I and II) and 1.64 nm (between areas II and III), while our method resolved these to be 0.56 and 1.62 nm, respectively, yielding absolute errors of only 0.02 nm. These results verify the feasibility of the proposed demodulation workflow and confirm its subnanometre accuracy in 2D material thickness profiling with a resolution of 0.56 nm, establishing the SPR holographic microscope as a viable alternative tool for nanoscale 2D material metrology. Notably, the proposed method is inherently suited for investigation of thin-film properties rather than thick samples, owing to the limited penetration depth of SPP (200 to 450 nm in the dielectric side in our SPR configuration). In addition, the demodulation workflow requires scanning of the incidence angle to determine θ_{SPR} , a process that typically lasts several seconds. Consequently, the method is not intended for applications involving rapid thickness variations, such as real-time monitoring of the in-situ growth of 2D materials.

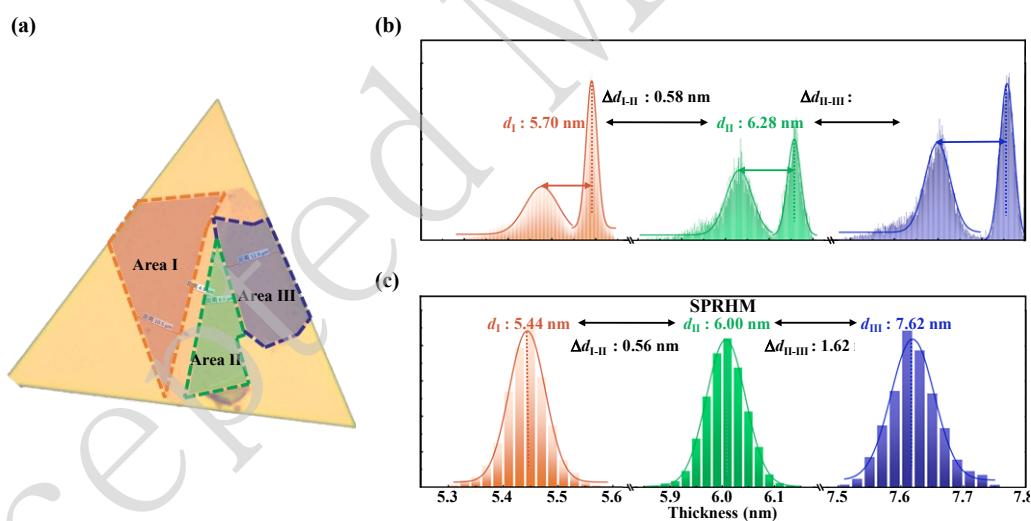


Fig. 5 Geometric thickness profiling of the graphene terrace. **a** Bright-field microscope image of the graphene specimen on the Au substrate. Different colours indicate areas of varying thickness. **b** Geometric thickness histogram in three steps obtained from AFM measurements with Gaussian fitting results. The AFM thickness quantification via height difference generates bimodal histograms, where peak separations directly yield the graphene–substrate height offset. **c** Geometric thickness histogram in three steps obtained from measurements by the SPR holographic microscope with

Gaussian fitting results.

Optical structure and opto-mechanical design of the microscope

The optical structure of the common-path objective-coupled SPR holographic microscope is shown in Fig. 6a²⁸. A linearly polarised laser beam with a wavelength of 632.8 nm is coupled into an optical fibre. The output beam from the fibre is expanded and then collimated as a plane wave using a negative lens (NL) followed by a collimating lens (CL). The collimated laser beam subsequently passes through a focusing lens (FL), polariser 1 (P1), and plate beamsplitter (BS), converging onto the back focal plane of a microobjective (MO). The MO outputs a plane wave, providing a wide-field illumination for the SPR excitation configuration. The light beam reflected from the metal interface is collected by the same MO. The reflected beam traverses the BS and passes through a tube lens (TL), Wollaston prism (WP), and polariser 2 (P2) in turn to generate off-axis holograms. Finally, the resulting hologram is recorded by a CCD camera (see details in Supplementary Information 5). P1 is oriented along the 45° direction to modulate the polarisation state of the incident light beam. By longitudinally moving the fibre, NL, CL, FL, and P1 assembly as a single unit via a motorised translation stage in the direction indicated by the arrow in Fig. 6a, a lateral position offset is introduced between the beam centre and optical axis of the MO. Consequently, the light beam emerging from the MO impinges on the metal–dielectric interface at an oblique angle.

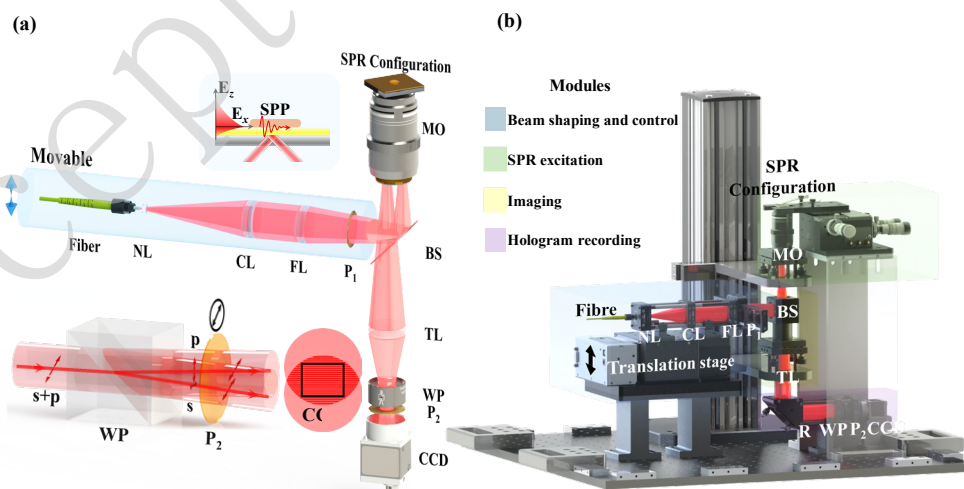


Fig. 6 Structure of the common-path objective-coupled SPR holographic microscope. **a** Schematic of the optical structure. The top inset schematically depicts the SPP excitation and corresponding

distribution of the evanescent electric field. The bottom inset describes the working principle of the hologram recording module. **b** Opto-mechanical structure design with four modules.

The opto-mechanical design, depicted in Fig. 6b, is modularised into four functional modules: beam shaping and control, SPR excitation, imaging, and hologram recording. Further details regarding the composition and functionality of the modules are presented in Supplementary Information 6. All modules are rigidly coupled to an optical breadboard with vibration-isolation tables. The modular opto-mechanical design enhances the system compactness while facilitating component replacement and upgrades. The use of standardised mechanical parts minimises cumulative assembly tolerances, leading to a significantly improved optical axis alignment precision. Strategically positioned vibration-isolation tables decouple critical modules from environmental disturbances, ensuring measurement stability. Finally, the entire microscope is carefully housed. The fully sealed enclosure substantially relaxes experimental environmental constraints and enables a robust deployment in nonlaboratory settings, thereby expanding potential application scenarios beyond conventional laboratory confines. Beyond the inherent advantages of SPRHM, the proposed versatile microscope features minimal opto-mechanical complexity, operational simplicity, and exceptional measurement stability to enable diverse applications. The assembly of the SPR holographic microscope and its key features are detailed in Supplementary Information 7.

Discussion

For RI measurements, SPR-based sensors have been widely investigated due to their distinct advantages of high sensitivity to RI and label-free detection capabilities. These attributes have enabled diverse applications spanning biomedical diagnostics³⁵, food safety control³⁶, and environmental monitoring³⁷. Conventional SPR sensor platforms typically employ angular³⁸ or wavelength³⁹ interrogation schemes; however, they face inherent limitations including a restricted sensitivity and reliance on a sophisticated optical instrumentation. Consequently, advanced SPR excitation configurations have emerged for enhancing the RI measurement performance and simplifying systems, including a multicore-flat-fibre-incorporated structure⁴⁰, graphene-based architecture exploiting hybrid circular/triangular resonators⁴¹, and metal-insulator-metal waveguides with maze-type

cavities⁴². Although current excitation configurations achieve an improved sensitivity, rapid response, and miniaturisation, their reliance on complex nanofabrication processes incurs prohibitive costs.

The intrinsic properties of 2D materials, including the electrical conductivity, optical absorption, and mechanical strength, exhibit strong thickness dependences⁴³. Moreover, critical physics phenomena such as interlayer coupling⁴⁴ and quantum confinement effects⁴⁵ require an atomic-level thickness precision. Thus, metrology tools with a high accuracy and high measurement throughput serve as a foundational metric ('ruler') for 2D material research, bridging fundamental properties with device applications while directly enabling performance breakthroughs. Various metrology techniques have been applied in the characterisation of 2D materials, such as AFM⁴⁶, scanning electron microscopy (SEM)⁴⁷, Raman spectroscopy⁴⁸, and ellipsometry⁴⁹. AFM and SEM offer a subnanometre precision but pose a potential damage risk to the specimen. In addition, the point-scanning approach suffers from a low throughput. Raman spectroscopy provides thickness-sensitive fingerprints but relies on empirical databases with a limited generalisability, and the measurement speed is rather low. Although ellipsometry provides noncontact thickness mapping of 2D materials, its reliance on wavelength or illumination angle scanning and high complexity in model fitting can potentially constrain the measurement throughput.

In this study, we present a Ag–Au bilayer SPR sensor incorporating a thickness optimisation algorithm to significantly enhance the practical RI measurement sensitivity. In addition, an angle-scanning thickness demodulation workflow implemented on our SPR holographic microscope enables high-throughput thickness profiling of 2D materials without requiring a prior empirical calibration. We further provide an explanation for the achieved ultrahigh sensitivity. The enhanced RI sensitivity originates from three key physical mechanisms. (i) An optimised Ag–Au bilayer SPR excitation configuration is employed to maximise the RI measurement sensitivity S . (ii) The integration of DHM with SPRM enables phase-based SPR sensing, providing a higher sensitivity than conventional intensity-based approaches. (iii) The implementation of the common-path interferometry geometry, along with the comprehensive mechanical stabilisation (vibration-isolation tables and sealed enclosure), effectively suppresses perturbations from mechanical vibrations and air turbulence. This

substantially reduces the phase measurement noise and allows the ultrahigh measurement sensitivity to be realised in practice. The enhanced thickness profiling resolution is enabled by the latter two mechanisms, i.e. phase-based SPR sensing and common-path interferometric noise suppression, combined with pixelwise thickness demodulation. Despite the efforts using the high-stability opto-mechanical design and robust demodulation algorithm to suppress the phase measurement noise, the photon shot noise has a dominant role in limiting the current measurement sensitivity, indicating that a state-of-the-art detector could further enhance sensitivity.

Conclusion

We introduced an optimised Ag–Au bilayer SPR excitation configuration and proprietary thickness demodulation workflow to achieve an ultrahigh-sensitivity measurement with respect to both RI and thickness. Rigorous experimental validations confirmed the ability to monitor RI variations of ethanol–water evaporation dynamics with a resolution of 2.58×10^{-7} RIU, as well as to perform accurate thickness profiling of a graphene specimen with a step height of 0.56 nm. Based on these advanced methods, we engineered a versatile SPR holographic microscope characterised by minimal opto-mechanical complexity, operational simplicity, and exceptional stability. The integrated motorised angular scanning mechanism enables flexible data acquisition, leading to an enhanced information throughput. As the SPR holographic microscope prototype bridges laboratory verification and practical applications, this technique establishes a new platform for noninvasive, label-free, wide-field, and high-throughput detection with an ultrahigh sensitivity. We anticipate progressive impacts across biological research, in situ nanomaterial inspection, and electrochemical studies.

Acknowledgements

This study was supported by National Natural Science Foundation of China (Grant Nos. 61927810, 62005219, and 62405246).

Author contributions

Lingke Wang: Conceptualisation, Data curation, Formal analysis, Methodology, Visualisation, Writing - original draft. **Jingyu Mi:** Formal analysis, Methodology, Validation. **Jiahao Li:**

Investigation, Resources, Validation. **Wenrui Li**: Data curation, Methodology, Resources. **Siqing Dai**: Funding acquisition, Investigation, Validation. **Jiwei Zhang**: Conceptualisation, Funding acquisition, Project administration, Writing - review & editing. **Jianlin Zhao**: Funding acquisition, Project administration, Supervision, Writing - review & editing.

Data availability

Data underlying the results presented in this paper are not publicly available at this time but may be obtained from the authors upon reasonable request.

Conflict of interests

The authors declare no conflicts of interest.

References

1. Zhou, X. L. et al. Surface plasmon resonance microscopy: from single-molecule sensing to single-cell imaging. *Angewandte Chemie International Edition* **59**, 1776-1785 (2020).
2. Homola, J., Yee, S. S. & Gauglitz, G. Surface plasmon resonance sensors: review. *Sensors and Actuators B: Chemical* **54**, 3-15 (1999).
3. Zayats, A. V., Smolyaninov, I. I. & Maradudin, A. A. Nano-optics of surface plasmon polaritons. *Physics Reports* **408**, 131-314 (2005).
4. Yeatman, E. & Ash, E. A. Surface plasmon microscopy. *Electronics Letters* **23**, 1091-1092 (1987).
5. Zeng, Q. et al. Dynamic single-molecule sensing by actively tuning binding kinetics for ultrasensitive biomarker detection. *Proceedings of the National Academy of Sciences of the United States of America* **119**, e2120379119 (2022).
6. Khochare, S. D. et al. Functional plasmonic microscope: characterizing the metabolic activity of single cells via sub-nm membrane fluctuations. *Analytical Chemistry* **96**, 5771-5780 (2024).
7. Zhai, C. H. et al. Precise identification and profiling of surface proteins of ultra rare tumor specific extracellular vesicle with dynamic quantitative plasmonic imaging. *ACS Nano* **17**, 16656-16667 (2023).

8. Zhang, P. F. et al. Plasmonic scattering imaging of single proteins and binding kinetics. *Nature Methods* **17**, 1010-1017 (2020).
9. Wu, G. et al. Dynamic imaging of interfacial electrochemistry on single Ag nanowires by azimuth-modulated plasmonic scattering interferometry. *Nature Communications* **14**, 4194 (2023).
10. Fang, Y. M. et al. Intermittent photocatalytic activity of single CdS nanoparticles. *Proceedings of the National Academy of Sciences of the United States of America* **114**, 10566-10571 (2017).
11. Liu, Z. W. et al. Flexible hyperspectral surface plasmon resonance microscopy. *Nature Communications* **13**, 6475 (2022).
12. Kuai, Y. et al. Label-free surface-sensitive photonic microscopy with high spatial resolution using azimuthal rotation illumination. *Science Advances* **5**, eaav5335 (2019).
13. Liu, Y. et al. Wide-field optical sizing of single nanoparticles with 10 nm accuracy. *Science China Physics, Mechanics & Astronomy* **64**, 294213 (2021).
14. Mandracchia, B. et al. Surface plasmon resonance imaging by holographic enhanced mapping. *Analytical Chemistry* **87**, 4124-4128 (2015).
15. Huang, B., Yu, F. & Zare, R. N. Surface plasmon resonance imaging using a high numerical aperture microscope objective. *Analytical Chemistry* **79**, 2979-2983 (2007).
16. Zeng, Y. J. et al. Wavelength-scanning surface plasmon resonance microscopy: a novel tool for real time sensing of cell-substrate interactions. *Biosensors and Bioelectronics* **145**, 111717 (2019).
17. Huang, Y. H. et al. Detecting phase shifts in surface plasmon resonance: a review. *Advances in Optical Technologies* **2012**, e471957 (2012).
18. Wu, S. Y. et al. Highly sensitive differential phase-sensitive surface plasmon resonance biosensor based on the mach–zehnder configuration. *Optics Letters* **29**, 2378-2380 (2004).
19. Huang, Y. H. et al. Phase sensitive SPR sensor for wide dynamic range detection. *Optics Letters* **36**, 4092-4094 (2011).
20. Shao, Y. H. et al. Wavelength-multiplexing phase-sensitive surface plasmon

- imaging sensor. *Optics Letters* **38**, 1370-1372 (2013).
21. Hu, C. Y., Zhong, J. G. & Weng, J. W. Digital holographic microscopy by use of surface plasmon resonance for imaging of cell membranes. *Journal of Biomedical Optics* **15**, 056015 (2010).
 22. Zhang, J. W. et al. Azimuthal scanning excitation surface plasmon resonance holographic microscopy. *Laser & Photonics Reviews* **18**, 2301013 (2024).
 23. Dai, S. Q. et al. Dual-wavelength surface plasmon resonance holographic microscopy for simultaneous measurements of cell-substrate distance and cytoplasm refractive index. *Optics Letters* **47**, 2306-2309 (2022).
 24. Mi, J. Y. et al. Thickness measurement of bimetallic film using surface plasmon resonance holographic microscopy. *Optics Express* **31**, 39415-39423 (2023).
 25. Kim, M. K. Phase microscopy and surface profilometry by digital holography. *Light: Advanced Manufacturing* **3**, 481-492 (2022).
 26. Li, S. P. & Zhong, J. G. Simultaneous amplitude-contrast and phase-contrast surface plasmon resonance imaging by use of digital holography. *Biomedical Optics Express* **3**, 3190-3202 (2012).
 27. Zhang, J. W. et al. A review of common-path off-axis digital holography: towards high stable optical instrument manufacturing. *Light: Advanced Manufacturing* **2**, 333-349 (2021).
 28. Zhang, J. W. et al. Compact surface plasmon holographic microscopy for near-field film mapping. *Optics Letters* **42**, 3462-3465 (2017).
 29. Dai, S. Q. et al. Real-time and wide-field mapping of cell-substrate adhesion gap and its evolution via surface plasmon resonance holographic microscopy. *Biosensors and Bioelectronics* **174**, 112826 (2021).
 30. Dai, S. Q. et al. Optical tweezers integrated surface plasmon resonance holographic microscopy for characterizing cell-substrate interactions under noninvasive optical force stimuli. *Biosensors and Bioelectronics* **206**, 114131 (2022).
 31. Dai, S. Q. et al. Label-free and dynamic monitoring of cell evolutions using wavelength-multiplexing surface plasmon resonance holographic microscopy. *Biomedical Optics Express* **14**, 2028-2039 (2023).

32. Haynes, W. M. CRC Handbook of Chemistry and Physics. 97th edn. (Boca Raton: CRC Press, 2016).
33. Polyanskiy, M. N. Refractiveindex.info database of optical constants. *Scientific Data* **11**, 94 (2024).
34. Bruna, M. & Borini, S. Optical constants of graphene layers in the visible range. *Applied Physics Letters* **94**, 031901 (2009).
35. Nguyen, H. et al. Surface plasmon resonance: a versatile technique for biosensor applications. *Sensors* **15**, 10481-10510 (2015).
36. Balbinot, S. et al. Plasmonic biosensors for food control. *Trends in Food Science & Technology* **111**, 128-140 (2021).
37. Estelmann, A. et al. An SPR-based in situ methane sensor for the aqueous and gas phase. *Analytical Chemistry* **96**, 16203-16214 (2024).
38. Zeng, Y. J. et al. A speckle-free angular interrogation SPR imaging sensor based on galvanometer scan and laser excitation. *Plasmonics* **14**, 1497-1504 (2019).
39. Yuk, J. S. et al. Characterization of surface plasmon resonance wavelength by changes of protein concentration on protein chips. *Sensors and Actuators B: Chemical* **94**, 161-164 (2003).
40. Rifat, A. A. et al. Highly sensitive multi-core flat fiber surface plasmon resonance refractive index sensor. *Optics Express* **24**, 2485 (2016).
41. Alsharari, M. et al. Enhanced sensing efficiency of ultra-narrow band graphene-based surface plasmon resonance refractive index sensor for biochemical applications and environmental monitoring. *Plasmonics* **20**, 1273-1284 (2024).
42. Majidi, Z., Ghanavati, M. & Karami, M. A. Multi-resonance plasmonic refractive index sensor based on maze-shaped resonators for biological applications. *Journal of Optics* **26**, 095002 (2024).
43. Tan, C. L. et al. Recent advances in ultrathin two-dimensional nanomaterials. *Chemical Reviews* **117**, 6225-6331 (2017).
44. Wilson, N. P. et al. Interlayer electronic coupling on demand in a 2D magnetic semiconductor. *Nature Materials* **20**, 1657-1662 (2021).
45. Yi, Y. et al. Recent advances in quantum effects of 2D materials. *Advanced*

Quantum Technologies **2**, 1800111 (2019).

46. Lee, C. et al. Measurement of the elastic properties and intrinsic strength of monolayer graphene. *Science* **321**, 385-388 (2008).
47. Hui, F. et al. Emerging scanning probe-based setups for advanced nanoelectronic research. *Advanced Functional Materials* **30**, 1902776 (2020).
48. Wu, J. X. & Xie, L. M. Structural quantification for graphene and related two-dimensional materials by Raman spectroscopy. *Analytical Chemistry* **91**, 468-481 (2019).
49. Yoo, S. & Park, Q. H. Spectroscopic ellipsometry for low-dimensional materials and heterostructures. *Nanophotonics* **11**, 2811-2825 (2022).